EUROfusion

EUROFUSION WPMST1–PR(15)31

M. Sertoli et al.

Two Dimensional Impurity Density Measurements in the Presence Saturated (m,n) = (1,1) Modes at ASDEX Upgrade

Preprint of Paper to be submitted for publication in Nuclear Fusion

This work has been carried out within the framework of the EUROfusion Consortium and has received funding from the Euratom research and training programme 2014-2018 under grant agreement No 633053. The views and opinions expressed herein do not necessarily reflect those of the European Commission.

Two dimensional impurity density measurements in the presence saturated (m,n)=(1,1) modes at ASDEX Upgrade

M. Sertoli, T. Odstrcil and the ASDEX Upgrade Team

Max-Planck-Institut für Plasmaphysik, Boltzmannstrasse 2, D-85748 Garching, Germany

E-mail: marco.sertoli@ipp.mpg.de

Abstract. A new method for the determination of 2D intrinsic tungsten density profiles in the presence of saturated MHD instabilities at ASDEX Upgrade is presented. For the first time the full decoupling of the impurity density from electron density and temperature contributions to experimental 2D SXR tomographic reconstructions in the presence of MHD can be performed. The analysis relies on a combination of SXR tomography with the reconstruction of 2D electron temperature profiles through harmonic decomposition of the 1D ECE electron temperature. The method is applicable to any saturated magnetic perturbation as long as the poloidal and toroidal mode numbers m and n are known, and if the concentration of the intrinsic tungsten is high enough to dominate the SXR signals. This method may help better understand the mitigation of tungsten accumulation by central ECRH which typically occurs in the presence of saturated $(m, n) = (1, 1)$ MHD activity. The analysis of the evolution of the intrinsic tungsten density in a typical ASDEX Upgrade discharge with central ECRH and saturated $(1, 1)$ modes is presented.

PACS numbers: 52.25.Os, 52.25.Xz, 52.30.Cv, 52.50.Sw, 52.55.Fa, 52.55.Tn, 52.70.Ds, 52.70.Gw

Keywords: tokamaks, impurities, ECE, MHD instabilities, internal kink, sawtooth, Fourier transform, ECR heating, data analysis

1. Introduction

Since its discovery in tokamak plasmas in the 1970s, the internal-kink MHD instability characterised by poloidal and toroidal mode numbers $(m, n) = (1, 1)$ has been mainly studied with the soft X-ray diagnostic (SXR) which measures all electromagnetic radiation emitted in an energy range typically $1 \rightarrow 20\ keV$ and the electron cyclotron emission diagnostic (ECE) which measures radial profiles of the electron temperature (see e.g. [1–18]). These diagnostics give important information *per-se* for the characterisation of the processes in action, but, due to the helical equilibrium arising in the presence of such instabilities, without any post-processing mainly provide only qualitative estimations of the evolution of the various quantities.

The application of two-dimensional tomographic reconstruction methods to the signals of the SXR diagnostic (see e.g. [3,7,9,19]) and rotation tomography techniques to data from 1D ECE [20, 21] or 1D fast-sweeping X-mode reflectometry [22] have enabled more quantitative analysis of the behaviour of the SXR plasma emission,

electron temperature and density in the presence of such modes. Imaging ECE diagnostics (ECEI, see e.g. [23–25]), delivering intrinsically 2D electron temperature maps, are also a very powerful tool to compare experimental data with theory of the structure and dynamics of $(1,1)$ modes, but have the drawback of covering only small fractions of the minor radius.

Regardless of these major advances in both diagnostic development and data analysis techniques, a quantitative characterisation of the behaviour of impurity densities in 2D during saturated $(1,1)$ modes or during the sawtooth crash is instead still missing. Due to the helical equilibrium arising in the presence of the $(1,1)$ mode, standard experimental methods for the determination of the impurity transport coefficients [26–32] or of the impurity density [33, 34] employing flux-surface-averaged quantities cannot be applied for a full characterisation of the processes in action.

This contribution presents a new method that enables the experimental characterisation of the mode-resolved 2D impurity density distribution in the presence of slowly evolving ($\gamma << \omega$ where γ is the growth rate and $\omega \neq 0$ the mode rotation frequency in the laboratory frame) or saturated MHD instabilities. The analysis relies on the combination of advanced SXR tomographic reconstructions [35] with 2D mode-resolved electron temperature profile reconstruction performed through harmonic decomposition of the 1D ECE electron temperature data [21]. The method is applicable if the investigated impurity dominates the SXR signals with respect to contributions from other impurities and the background ion, as is the case for W in the plasma centre of most ASDEX Upgrade discharges. Any magnetic perturbation can be studied as long as the mode numbers (m and n) of the instability are known. Previous studies have investigated the perturbations in the electron temperature and in the SXR signals separately or side-by-side, but the present work shows for the first time a full decoupling of the impurity density from electron density and temperature contributions in 2D SXR tomographic reconstruction in the presence of MHD activity. One of the major applications of this method is the characterisation of the dynamics of the mitigation of W accumulation by central ECRH [33, 36–39], at ASDEX Upgrade usually occurring in the presence of long-lived $(1,1)$ modes in-between sawtooth crashes. Further correlation between the occurrence of $(1,1)$ MHD activity and modification of impurity transport has been documented [34, 40–42] but a mode-resolved picture of the processes in action is still missing.

The method for the determination of the intrinsic W density [34] is reviewed in section 2, extending it to 2D. A review of the 2D mode-resolved electron temperature remapping technique [21] is also given, extending it so to perform phase-locking with the SXR tomographic reconstructions. A typical ASDEX Upgrade H-mode discharge with central ECRH and long lasting $(1,1)$ modes (in-between sawtooth crashes) is described in section 3. In section 4, the boundary conditions for the application of the method are verified for the given example, the characteristics of the MHD activity are analysed and the 1D W density is calculated as explained in [34]. The 2D mode-resolved electron temperature and W density profiles for one sawtooth cycle are analysed in section 5. A summary and an outlook are given in section 6.

2. Method for the evaluation of the 2D mode-resolved W density

If one impurity dominates the SXR emission as is the case for W in the plasma centre for most AUG discharges, its density n_W can be evaluated from the experimental SXR

emissivity ϵ_{exp}^{sxr} through the simple equation:

$$n_W(\mathbf{r};t) \propto \frac{\epsilon_{exp}^{sxr}(\mathbf{r};t)}{n_e(\mathbf{r};t)\ L_W^{sxr}(\mathbf{r};t)} \tag{1}$$

where n_e is the electron density and $L_W^{sxr} = \sum_q f_{W,q}\, k_{W,q}^{sxr}$ the radiation loss parameter (also called *cooling factor*) filtered according to the filter function of the SXR diagnostic. All quantities in equation 1 are defined in the three-dimensional space $\mathbf{r}$ of the tokamak and are a function of time. The application of this equation requires that a few boundary conditions be satisfied.

2.1. Boundary conditions

For tokamak-relevant electron densities (several $10^{19}\ \ m^{-3}$), the emissivity rate coefficients $k_{W,q}^{sxr}$ are a function of the electron temperature only. The fractional abundances $f_{W,q} = n_{W,q}/n_W$ of the various ionization stages q are instead a function of both electron temperature and transport. Depending on ionization and recombination time scales in comparison to the transport time scales, the dependence of transport may be more or less relevant. As already argued in [34], in the sensitivity range of the SXR diagnostic installed at AUG (photon energy $\sim 1 - 20\ keV$) the W contributions come mainly from spontaneous line-emission occurring from electron-impact excited states. The lower photon energy detection limit of 1 keV therefore approximately corresponds to an electron temperature limit of $T_e > 1\ keV$. Accounting for possible inaccuracies in the SXR filter-function at the lower cut-off energy but trusting its shape at higher photon energies, L_W^{sxr} can be assumed to be known with precision within a conservative detection limit of $T_e > 1.3 - 1.5\ keV$. For standard AUG plasmas, this limit is well inside the pedestal top where ionization and recombination rates of tungsten are typically much higher than the transport time-scales. In these cases, the fractional abundances can therefore be modelled using local ionization equilibrium [43]. This further simplifies the application of equation 1 since no information on impurity transport is necessary for the calculation of the fractional abundances and the radiation loss parameter L_W^{sxr} becomes a function of the electron temperature only. Finally, if the SXR channels used for the analysis have a correct relative calibration, the shape of the W-density profile computed through equation 1 will be correct. Its absolute value can then be rescaled through a multiplication constant estimated by comparing the result with independent measurements from calibrated passive tungsten vacuum-ultra-violet (VUV) spectroscopy. Details on the comparison and rescaling are given in [34] and reviewed in section 4 for clarity.

For the calculation of flux-surface averaged W densities, a 1D Abel inversion of SXR LoSs and radial profiles of the electron temperature and density are sufficient for the application of equation 1. This can be easily employed in the absence of MHD activity (i.e. in axisymmetric tokamak geometry) or averaging over the mode rotation [34]. If mode-resolved profiles are to be calculated, equation 1 has instead to be applied in 2D on a poloidal cross-section of the tokamak. Two-dimensional mode-resolved maps of the electron density and temperature are therefore required, the former for direct introduction in equation 1, the latter for the calculation of a 2D map of the radiation loss parameter L_W^{sxr}. These 2D maps can be obtained applying rotation tomography techniques to 1D measurements such as those provided by ECE for the electron temperature and fast-sweeping X-mode reflectometry for the electron density.

2.2. 2D mode-resolved electron temperature profiles

A 2D mode-resolved map of the electron temperature can be obtained through a recently developed method relying on harmonic decomposition of the 1D ECE measurements in Fourier components evaluated through continuous short time Fourier transform (STFT) [44, 45]. The method requires only prior knowledge of the mode numbers (m, n) of the MHD instability and of the non-perturbed axisymmetric magnetic equilibrium. An extensive explanation can be found in [21] and is reviewed here for clarity.

The mode-resolved 2D electron temperature map at time t_{ECE} and at the toroidal position of the ECE diagnostic ϕ_{ECE} can be expressed mathematically through the following equation:

$$T_e(\rho_n; \vartheta^*, t_{ECE}) = \langle T_e(\rho_n; t_{ECE}) \rangle + \sum_{k=1}^{N} \delta T_{e,k}(\rho_n; t_{ECE}) \cdot \cos[m_k \vartheta^* + \varphi_k^{rm}(\rho_n; t_{ECE})] \quad (2)$$

where ρ_n is radial position of ECE channel n, ϑ^* the straight-field-line poloidal remapping angle (see e.g. [46]) and t_{ECE} is the ECE time-point used as centre for the Gaussian window function employed for the execution of the STFT. The right hand side of equation 2 includes the unperturbed electron temperature profiles $\langle T_e \rangle$ (the continuum components of the Fourier transform), the perturbation amplitudes $\delta T_{e,k}$ and phases φ_k^{rm} of each ECE channel (re-mapped as will be explained shortly) and each harmonic component k of poloidal mode number m_k. The sum is performed over all harmonic components which are accounted for, i.e. all those exceeding the noise level, typically $N = 3$ for $(1, 1)$ modes.

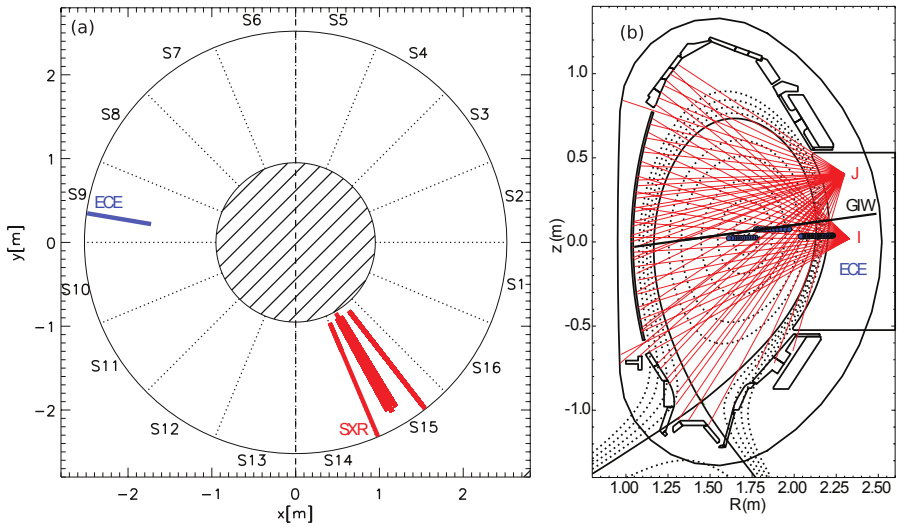

Figure 1. Toroidal (a) and poloidal (b) cross-sections of AUG with the measurement positions of the ECE (in sector 9), of the SXR (in sector 15) and GIW diagnostics (poloidal projection only). In (a) the LoS of SXR cameras *H, I, J, K, L, M, F* are shown; in (b) those from cameras *I* and *J* only for clarity.

Since the ECE channels do not measure exactly radially (figure 1a and 1b), the phase φ_k evaluated through the STFT includes a geometrical component which depends on the channel's position on the poloidal plane. This is accounted for by re-mapping φ_k to a reference poloidal angle, e.g. to the low-field-side (LFS) mid-plane ($\vartheta = \vartheta^* = 0$):

$$\varphi_k^{rm}(\rho_n; t_{ECE}) = \varphi_k(\rho_n; t_{ECE}) - m_k \vartheta^*(\rho_n, t_{ECE}) \tag{3}$$

where $\vartheta^*(\rho_n, t_{ECE})$ is the straight-field-line poloidal angle of the ECE channel n measuring at the radial position ρ_n. Since ρ_n depends on the position of the magnetic axis, equation 3 depends on time as well.

With this phase correction, equation 2 yields a 2D electron temperature map in the mode phase at the time t_{ECE} and at the toroidal location of the ECE antennas ϕ_{ECE}. Due to the constance of T_e on iso-flux surfaces, this profile can be remapped to an arbitrary toroidal location. This may not be the case for W since, due to its large mass, it is subject to poloidal asymmetries. The evaluation of the W density through equation 1 therefore requires that the 2D mode-resolved electron temperature for the calculation of the radiation loss parameter L_W^{sxr} is reconstructed at the time of the SXR tomographic reconstruction t_{SXR} and at the average toroidal location of the SXR cameras $\langle \phi_{SXR} \rangle = 300.12^\circ \pm 5.4^\circ$ (accounting for all cameras in sector 15 as shown in figure 1a). The LFS-remapped phase φ_k^{rm} in equation 2 and 3 must therefore further be corrected accounting for the phase shifts due to both time differences between ECE and SXR ($\Delta t = t_{SXR} - t_{ECE}$) and the different toroidal locations of the diagnostics ($\Delta\phi = \phi_{ECE} - \phi_{SXR}$):

$$\varphi_k^{rm,SXR}(r; t_{ECE}) = \varphi_k(r; t_{ECE}) - m_k \vartheta_r^* - (k\,\omega_1\,\Delta t + n_k \Delta\phi) \tag{4}$$

where ω_1 is the first harmonic frequency of the mode in the laboratory frame and n_k and the toroidal mode number of harmonic k.

2.3. 2D mode-resolved electron density profiles

The last ingredient missing for the application of equation 1 is a 2D mode-resolved map of the electron density. This can be evaluated using the same method used for the electron temperature or the rotation tomography developed in [20] which has been recently applied to fast-sweeping X-mode reflectometry data in Tore Supra [22] for the reconstruction of 2D mode-resolved electron density profiles. A similar reflectometry diagnostic has been recently been installed at AUG but, since it measures only up to $n_e \sim 5 \cdot 10^{19}\ m^{-3}$, its data was not available for the discharges of interest to this study. For this reason, the perturbation caused by the MHD instability in the electron density will be neglected and only the mode-averaged profiles will be used for the evaluation of the W density. As will be soon clear, this is a tolerable approximation since the electron density profiles are relatively flat in the region of interest.

3. Description of the experiment

The example reported is that of AUG discharge # 31114 executed in June 2014. This is a typical AUG lower-single-null H-mode discharge (flat-top geometry as in figure 1b) with $I_p = 1\ MA$, $B_t = -2.5\ T$, externally heated with $P_{NBI} = 7.5\ MW$ of neutral beam injection and $P_{ECRH} = 1.4\ MW$ of electron cyclotron resonance heating. The ECRH power is delivered using two gyrotrons providing $\sim 0.7\ MW$

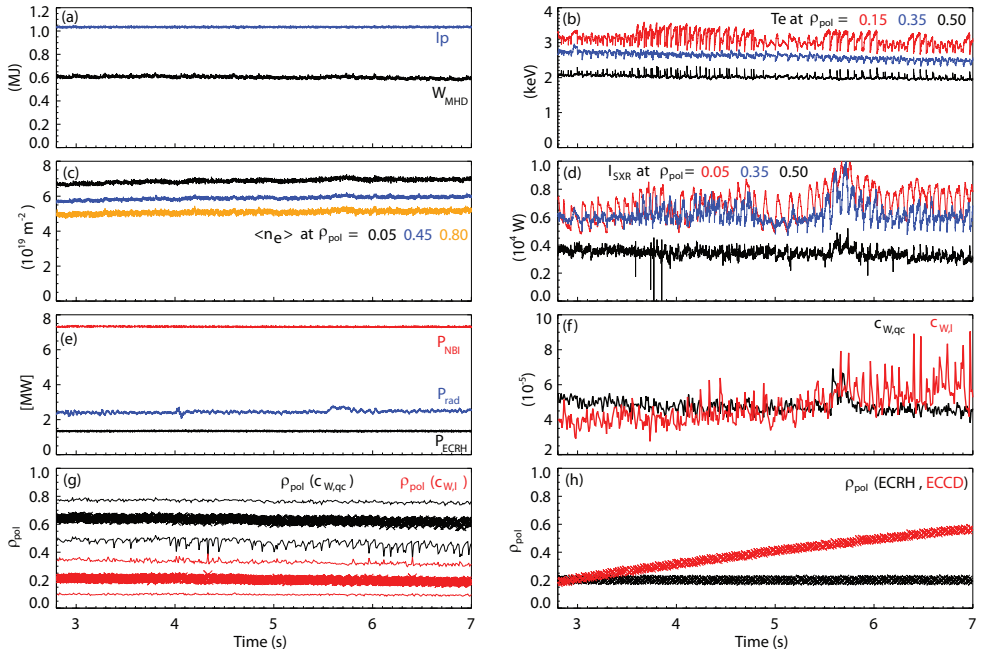

Figure 2. Main plasma parameters of AUG discharge # 31114: (a) I_p in blue, W_{MHD} in black; (b) electron temperature from ECE at 3 different radii (labelled on plot); (c) DCN interferometer LoS-averaged electron density (impact parameter labelled on plot); (d) brightness of 3 LoS of SXR camera I (impact parameter labelled on plot); (e) NBI (red) and ECRH (black) injected heating power, total radiated power (blue); (f) W concentration measurements from GIW; (g) their radial location (crosses) and width of averaging volume (continuous lines); (g) radial deposition position of the two gyrotrons (heating in black, current drive red).

each. The first one is used for heating only (perpendicular injection) and deposits at a fixed radial position $\rho_p^H \sim 0.2$ (black in figures 2h, 3a and 3b). The second one is adjusted for co-ECCD and its radial deposition position is linearly scanned in range $\rho_p^{CD} \sim 0.2 \rightarrow 0.6$ (red in figures 2h, 3a and 3b). The poloidal movement of the mirror used to perform this scan results in a slight variation of the toroidal inclination angle in range $\phi = -8° \rightarrow -6°$ leading to a total driven current $I_{CD} \sim 11 \rightarrow 5\ kA$. The deposition positions of the two gyrotrons as given in figure 2h are evaluated from the real-time version of the TORBEAM code [47, 48]. The gyrotron deposition positions, as well as all other radial coordinates used in this contribution, are given in normalised poloidal flux radial coordinates $\rho_{pol} = \sqrt{(\psi - \psi_a)/(\psi_s - \psi_a)}$, where ψ is the poloidal flux and the indices s and a refer to the separatrix and magnetic axis respectively. The subscript *pol* will be omitted from now on.

This heating setup allows for a modification of the sawtooth period [49] as well as of the MHD activity occurring in-between sawtooth crashes (figures 2 and 4), while keeping the sawtooth-averaged kinetic profiles as constant as possible (figure 5). The deposition position scan does not lead to any detectable change in the plasma energy (black in figure 2a) or in the total radiated power (blue in figure 2f). The

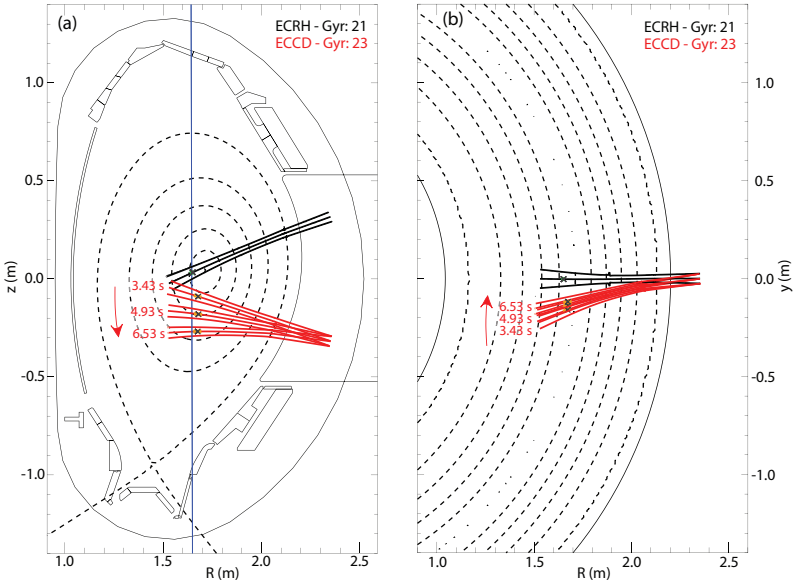

Figure 3. ECRH (gyrotron 21, in black) and ECCD (gyrotron 23, in red) poloidal and toroidal injection geometry for three different times (labeled in red) during the flat top of discharge # 31114 evaluated through TORBEAM [48]. Crosses along the beam path show the centre of deposition.

LoS integrated electron density moderately increases in time ($\sim 5\%$ over 4 seconds) identically for all LoS of the DCN interferometer (i.e., no changes in the profile shape, figure 2c) while the electron temperature (from ECE diagnostic data) decreases slightly ($< 8\%$ over 4 seconds) inside $\rho \sim 0.4$ (figure 2b).

As is already clear from the electron temperature and the SXR time traces (figure 2b and 2d, respectively), the structure of the sawtooth cycles is instead significantly affected. The LoS-integrated W concentration measurements of the grazing incidence spectrometer (GIW) [34,50] also show considerable variations (figure 2f). Not accounting at present for the modifications due to the sawtooth crashes, while the baseline of the *edge* concentration $c_{W,qc}$ (from the quasi-continuum spectral features of ionization stages $W^{27+} \rightarrow W^{35+}$, black in figure 2f) remains approximately constant, the one of the more *central* value $c_{W,l}$ (from spectral lines of ionization stages $W^{41+} \rightarrow W^{45+}$, red in figure 2f) increases of $\sim 50\%$. Since the electron temperature profile does not undergo significant changes in the region of integration of the two measurements (figures 2b and 5a), the average radial position of both concentration measurements does not change considerably during the whole time range: $\rho(c_{W,qc}) \sim 0.6$ and $\rho(c_{W,l}) \sim 0.2$ (crosses in figure 2g with the same colour code as figure 2f). The upper and lower boundaries of these radial positions (continuous lines in figure 2g) give the width of the emission shell participating in each measurement, i.e. represent the region of plasma over which the concentration is averaged. The W concentration can therefore be said to evolve *on average* from a hollow profile at 3 s to a peaked one at 7 s. Refer to [34] for details of the calculation of the radial position of the GIW measurements.

4. Tungsten density profile evolution from SXR (1D)

Before proceeding with the 2D mode-resolved reconstruction of the W density described in section 2, the boundary conditions explained in section 2.1 must be verified. As explained in [34], this can be done by evaluating the W density from SXR 1D Abel-inverted profiles using equation 1 and comparing the results with the independent measurement of the GIW spectrometer.

4.1. Verification of boundary conditions

Equation 1 has therefore been applied in one dimension using SXR cameras I and J (red LoS in figure 1b) assuming W as sole responsible element for the SXR emission. The electron temperature and density profiles used for the calculation come from integrated data analysis (IDA) fits [51] of ECE [52] for the electron temperature, Li-beam [53] and the DCN interferometer [54] for the electron density. The EQI equilibrium reconstruction (evaluated employing only magnetic measurements) has been employed for the mapping of all quantities. Since this analysis is averaged over mode rotation, all quantities of interest (SXR brightness, electron density and temperature) have been averaged over 10 ms, corresponding to ~ 100 mode rotations (mode frequencies in the laboratory frame $\geq 10\ kHz$ throughout the whole time-range of interest, figure 4b).

Since the most recent modelling of W spectra is still showing some discrepancies with the experimental data [50], only the shape of the SXR-filtered radiation loss parameter will be assumed trustworthy. As performed in [34], a post-processing calibration factor has been evaluated by simulating the GIW concentration measurement using the SXR-evaluated W density and the IDA electron density profiles, and comparing this result with the independent values given by the GIW spectrometer. The cross-calibration factor is then the ratio $\left\langle c_{W,l}(t)/c^{sxr}_{W,l}(t) \right\rangle$ averaged over the whole time-range of interest, where $c_{W,l}(t)$ is the GIW spectrometer measurement and $c^{sxr}_{W,l}(t)$ the simulated one using the SXR-evaluated W density (refer to [34] for further details). The post-rescaling comparison of the *central* measurement $c_{W,l}$ is shown in figure 4a, the GIW as a continuous black line, the SXR as dashed black line with red error bars. The error bars on the SXR-evaluated W concentration result from a full propagation of errors of the uncertainties from the Abel inversion of the SXR LoS (assuming a conservative 10% error on the SXR data accounting for possible cross-calibration issues between channels), from the electron density and temperature (see [34] for further details). The time evolution of the two signals matches very well within the experimental uncertainties for the whole time-range, both in the global evolution ($\sim$ 50% increase in the baseline from 3 to 7 seconds in the discharge) as well as in the fluctuations due to sawtooth-cycling. The boundary conditions required for the application of equation 1 outlined in section 2.1 are therefore verified for the present case for the whole time-range of interest.

Figure 4 has been divided into three time-windows depending on the ECCD deposition position with respect to the sawtooth inversion radius (determined from ECE data). This is located at $\rho_{inv} \sim 0.3$ at the start of the deposition position scan, is pushed to larger radii while the ECCD deposition position approaches the $q = 1$ surface ($\rho_{inv} \sim 0.35$ at 3.8 s, $\rho_{inv} \sim 0.4$ at 4.8 s) and finally shrinks back to ~ 0.3 when the ECCD passes the $q = 1$ surface (occurring approximately at 5.0 s) and remains stable at that value while the ECCD proceeds further outwards. The W

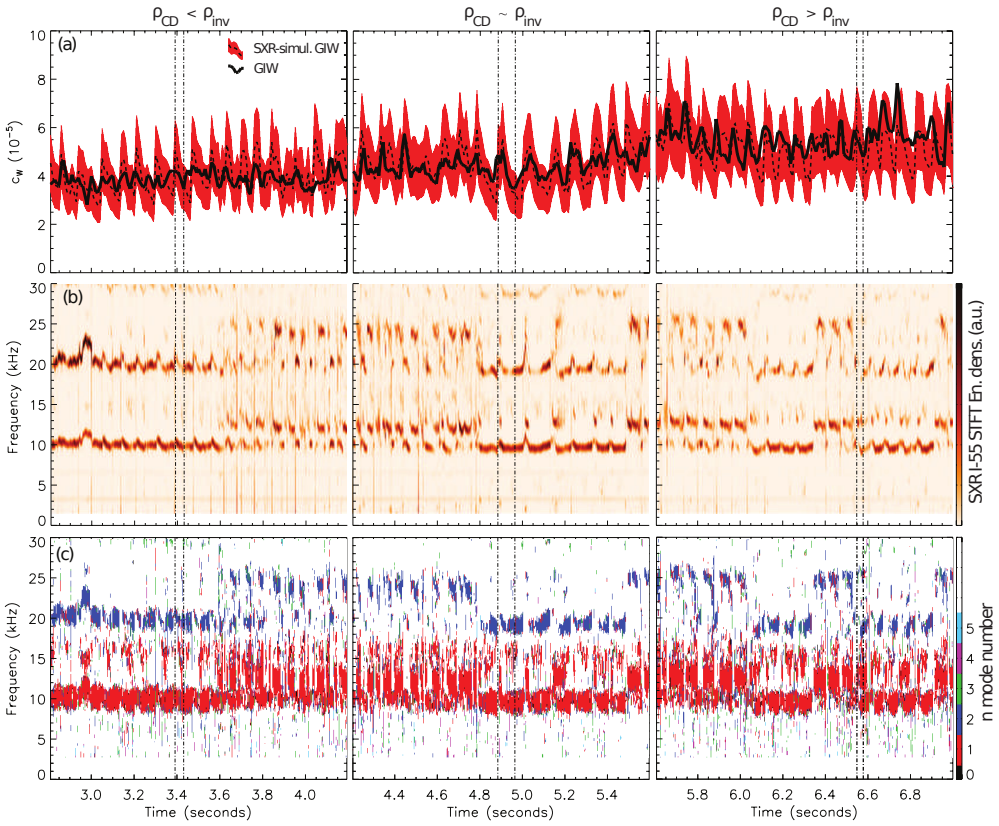

Figure 4. (a) most central tungsten concentration measurement $c_{W,l}$ of the GIW spectrometer (thick black lines) compared to the synthetic GIW W-concentration using the SXR-evaluated W density (black dashed lines with red error bars) throughout the flat-top of discharge #25447. (b) spectrogram of the SXR channel $I55$ (most central LoS of camera I). (c) toroidal mode numbers of the modes evaluated from the phase shift of magnetic coils $B31-03$ and $B31-12$.

concentration is almost constant until the ECCD is completely outside of the $q=1$ surface (at $\sim 5.3\ s$), time at which the baseline of the $c_{W,l}$ concentration is subject to an increase of $\sim 50\%$. Its value then remains approximately constant until the end of the time-range of interest. The position of the $q=1$ surface has been estimated assuming $\rho_{inv} \sim \sqrt{2}\rho_{q=1}$. This rough estimate is justifiable since the relative position of the $q=1$ surface and the inversion radius are expected to be constant throughout the whole time range of interest, the electron temperature profile undergoing only slight modifications in both shape and absolute value during the discharge.

The effects of the ECCD deposition position scan on the MHD activity in-between sawtooth cycles are clearly visible in the spectrogram of SXR LoS 55 of camera I (figure 4b). Modes are present in-between sawtooth crashes throughout the whole time-range, the main mode activity occurring at $\sim 10\ kHz$. A second, higher frequency (at $\sim 13\ kHz$) appears around $3.6\ s$, is almost completely suppressed at $4.8\ s$ but reappears between $5.4 \rightarrow 6.0\ s$ and again around $6.4\ s$. From the initial $\sim 50\ ms$,

the sawtooth period increases to $\sim 120\ ms$ around $5\ s$. After the ECCD crossing of the inversion radius it decreases to $\sim 70\ ms$, approaching $\sim 60\ ms$ at the end of the time-range of interest. Both the 10 and the 13 kHz modes are $(m, n) = (1, 1)$ modes. The poloidal mode number has been identified from the structure of the oscillations in the SXR signals (not shown), the toroidal one from the phase differences between magnetic coils having the same location on the poloidal plane, but at different toroidal positions along the torus. Figure 4c shows the toroidal mode number evaluated using the pair of coils $B31 - 03$ and $B31 - 12$, which are positioned at $\Delta\phi \sim 57.5°$ from one another toroidally and therefore sensitive to toroidal mode numbers up to $n = 6$ (its multiplicity due to the coil spacing $360°/\Delta\phi$) without the need of any complex mode-number fitting routine. Figure 4c also shows that the higher harmonics of these frequencies are $(m, n) = (2, 2)$ modes.

4.2. Sawtooth resolved profiles in the different phases

Since the boundary conditions for the application of the method are satisfied, the SXR density profiles can now be used to radially resolve the W density in individual sawtooth cycles occurring in the different phases of the discharge. One sawtooth period is analysed in each of the three phases outlined in the previous section (*inside*, *close-to* and *outside* of ρ_{inv} as in figure 4). For each phase, two time points per period have been chosen to show the variations occurring within one sawtooth cycle: one just after the sawtooth crash and one shortly before the next crash occurs (time-points shown as vertical dashed lines in the plots in figure 4).

The profiles of electron temperature, electron density (both from IDA fits), toroidal rotation from charge exchange recombination spectroscopy (CXRS) measurements on boron V and of the W density for these time points are shown in figure 5a-d, respectively. The exact times of the profiles are labelled on the top plots. The deposition position of the ECRH and ECCD as calculated by the TORBEAM code [48] is also shown using the same colour code as the profiles (just after a sawtooth crash in black, at the end of the cycle before the next crash occurs inred). Full circles and triangles in figure 5d show the *central* and *edge* W concentration measurements of the GIW spectrometer, respectively, multiplied by the electron density averaged over the radial range of integration of the measurement $\langle n_e(\rho(c_{W,l}))\rangle$. This radial range of integration is shown as a horizontal line while the vertical error bar represents a conservative estimate of 20% uncertainty to account for discrepancies between experimental and modelled W spectra.

The match between the SXR-evaluated W density profiles and both GIW measurements is satisfactory for all time points considered. The average increase of $\sim 50\%$ in *central* W density already discussed in the previous sections is found to come mainly from radii located around $\rho \sim 0.3 - 0.4$. The values inside this radius undergo instead a strong modulation due to the sawtooth crashes which are *inverted* with respect to typical crashes (as already shown for AUG plasmas in [55]), i.e. the W density flattens at the crash as usually observed (black profiles in figure 5c), but is hollow (instead of peaked) at the end of each period just before the next crash occurs (red profiles in figure 5c). The W density at the plasma centre at the end of the sawtooth period is for all time-points $n_W \sim 2 \cdot 10^{15}\ m^{-3}$, but the difference between pre and post crash phases increases when the ECCD deposition is moved further outwards. If contributions from deuterium and low-Z impurities are accounted for assuming $Z_{eff} = 1.3$ constant along the whole radial range, the resulting profiles

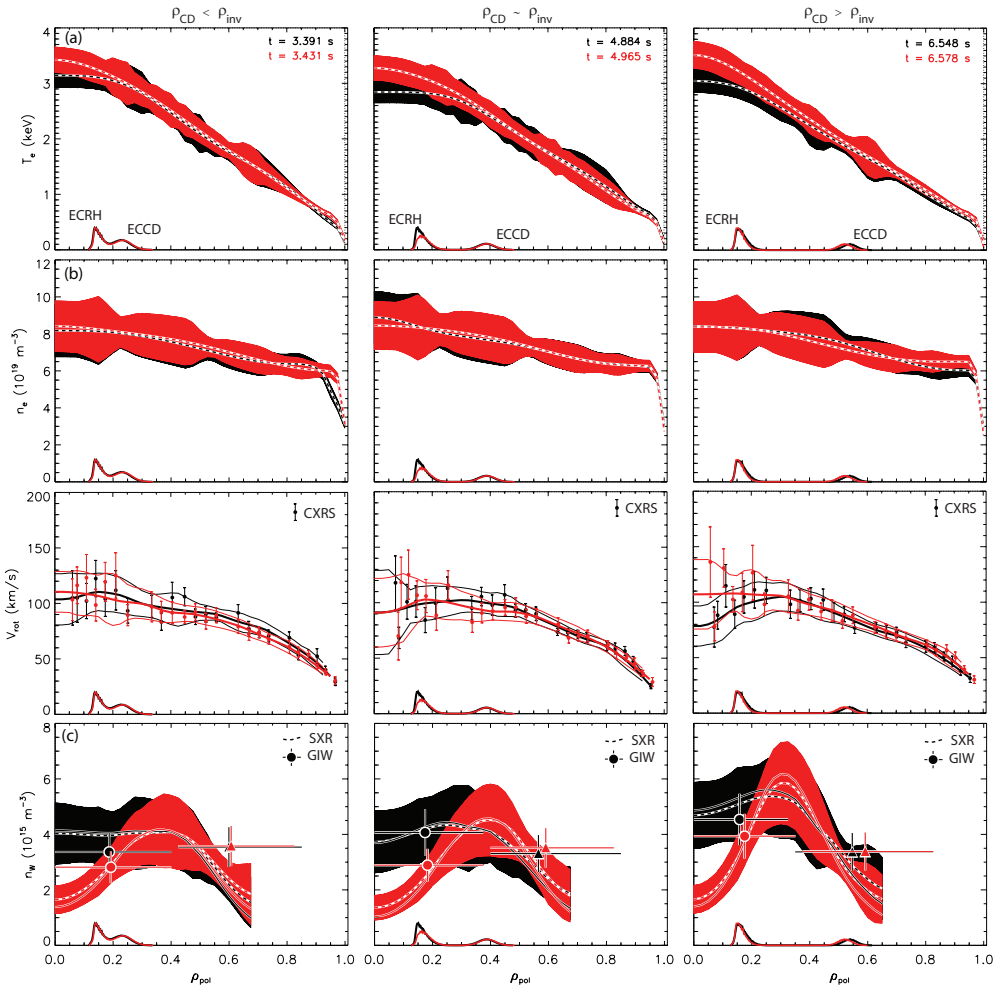

Figure 5. Profiles of: (a) electron temperature and (b) electron density from IDA fits, (c) toroidal rotation from CXRS measurements of boron *V*, (d) W density from SXR for the time-points labeled on plots (a) and shown as vertical dashed lines in figure 4, in black times occurring just after a sawtooth crash, in red those at the end of the sawtooth period, just before the next crash. Full circles and triangles in (d) are the GIW concentration measurements multiplied by $\langle n_e(\rho(c_{W,t}))\rangle$. Full lines without error bars in (d) show the W density evaluated accounting for main ion and low-Z impurity contributions to the SXR emissivity (assuming $Z_{eff} = 1.3$ constant along the radius.)

(continuous lines without error bars in figure 4c) fall within the error bars of the W-only profiles.

The electron temperature shows a moderate modulation due to the crashes, while the electron density seems to be almost unaffected within the measurement uncertainties. Since the error bars of the W density include the propagation of errors of both electron temperature and density profiles, the possibility of hollow electron

density profiles (within the measurement uncertainties) are already accounted for in the error bars. The toroidal rotation measurements from CXRS, while not being optimal and exhibiting a relatively large scatter, do not show considerable variations.

5. Mode-resolved 2D W density profiles

Now that the boundary conditions for the application of the method have been verified, the mode-resolved 2D W density profiles can finally be calculated using the method explained in section 2.2. The sawtooth cycle in time range $4.88 \rightarrow 5.00\ s$ with $\rho_{CD} \sim \rho_{inv}$ for which the 1D profiles have been examined (central plots in figure 5) will be investigated. Since the first step for this computation is the estimation of the 2D electron temperature profiles, the quality of this reconstruction will be first of all analysed.

5.1. Electron temperature reconstruction through STFT

The ECE diagnostic at AUG comprises three different mixers (the three rows of channels plotted in figure 1b as full blue circles) which exhibit different electronics for the data acquisition. The most central mixer has shown calibration problems with respect to the other mixers so only the latter two have been used for the 2D electron temperature reconstruction. This leads to a radial detection limit $\rho > 0.16$. In order to avoid any inconsistency in the data analysis, no attempt to extrapolate the electron temperature profiles to smaller radii has been carried out.

Using a maximum-search algorithm on the energy density of the STFT, the amplitude and phase information of the first three harmonics of the saturated mode have been extracted from the Fourier transform of each ECE channel and for each time-point in the window of analysis (see [21] for details on the estimation of the amplitude from the energy density of the STFT). The amplitude of all ECE channels as well as the cosine of the cross-phases of all ECE channels with respect to the most central one are shown in figure 7g and 7h for $t \sim 4.982\ s$, respectively. As visible in the time evolution of two ECE channels (figures 6a and 6b) and in their spectrogram (figures 6c and 6d), this time-point (dashed vertical line) is in the phase of mode saturation, the sawtooth crashes occurring at $t \sim 4.88\ s$ and $t \sim 5.00\ s$.

The quality of the reconstruction can be proven by re-building the time evolution of each channel using the information derived from the STFT, i.e. the continuum component of the Fourier transform $\langle T_e \rangle$, the oscillation amplitudes $\delta T_{e,k}$ and phases φ_k. This is shown in figure 7 for four ECE channels. As is clear from the comparison of the ECE data (black dots with error bars) and the reconstruction (thick continuous red line) as well as from the residuals $(data - fit)/error$ (where fit is the reconstructed signal and $error = 3\%$ the assumed ECE data uncertainty), the reconstruction matches very well the experimental data. The time range shown corresponds to $4\sigma_t$, where σ_t is the width of the Gaussian window function used for the STFT. This also gives an estimate of the time-resolution of the method for the present application, roughly $0.4\ ms$. As stated in [21], since the Gaussian window function has to include at least a few oscillations in order to deliver trustworthy amplitude and phase information, the reconstruction of the 2D profiles has to be limited to times where the oscillation frequency and its amplitude are approximately constant inside this time window. This can be quantified by calculating the mean squared weighed

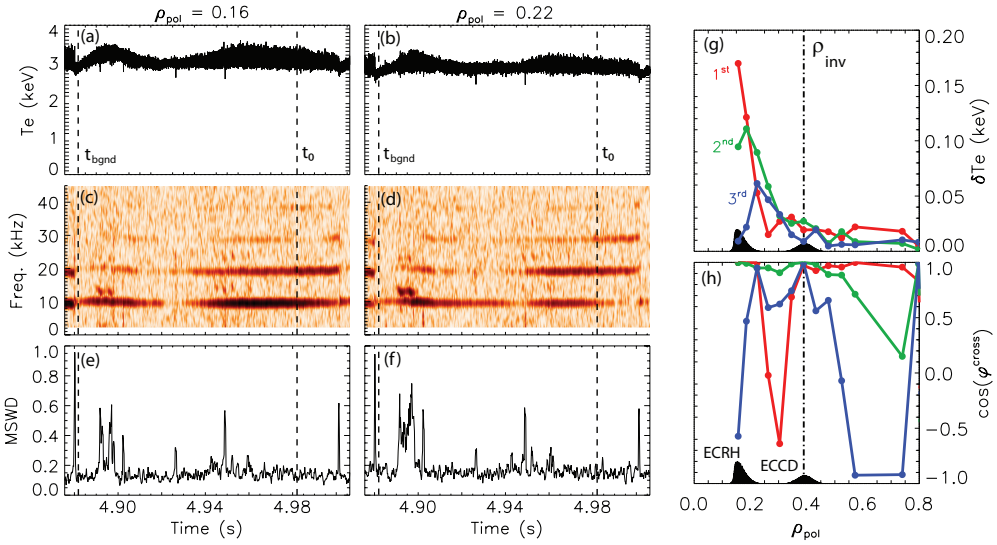

Figure 6. Time evolution of two ECE channels (a and b, radial position labeled on plot) for the sawtooth period under analysis; their spectrogram (c and d); the mean squared weighed deviation of their time-evolution reconstruction from STFT vs. the experimental data (e and f). The radial profiles of the oscillation amplitude and cosine of the cross-phase of all channels with respect to the most central one (g and h respectively), at $t_0 = 4.982\ s$. The different colours correspond to different harmonic components (as labeled), the dash-dot vertical line is the position of the inversion radius. The deposition position of ECRH and ECCD are also shown.

deviation for all channels:

$$MSWD = \frac{1}{(n-1)} \sum_{i=1}^{n} \frac{(d_i - f_i)^2}{e_i^2} \tag{5}$$

where $d = data$, $f = fit$ and $e = error$, and analysing only those time-points where this value is ≤ 1 (shown for two channels in figures 6e and 6f).

5.2. 2D mode-resolved profiles

Confident that the boundary conditions for the computation are satisfied and that the ECE data reconstruction is reliabile, the mode-resolved 2D electron temperature and W density can finally be computed. Only the saturation phase will be analysed, since what is of interest here is to resolve the W density in the non-axisymmetric equilibrium due to the presence of the helical structure of the saturated $(1, 1)$ mode. The time-points chosen are:

- $t_1 = 4.882\ s$: just after the sawtooth crash at the beginning of the analysed cycle for reference (equal to t_{bgnd} as labelled in figures 6a-b)
- $t_2 = 4.982015\ s$, $t_3 = 4.982030\ s$, $t_4 = 4.982043\ s$, $t_5 = 4.982058\ s$: during mode saturation, all occurring within a window of 43 μs around $t_0 = 4.982$ (as labelled in figures 6a-b) for which the amplitude and phase of the electron temperature

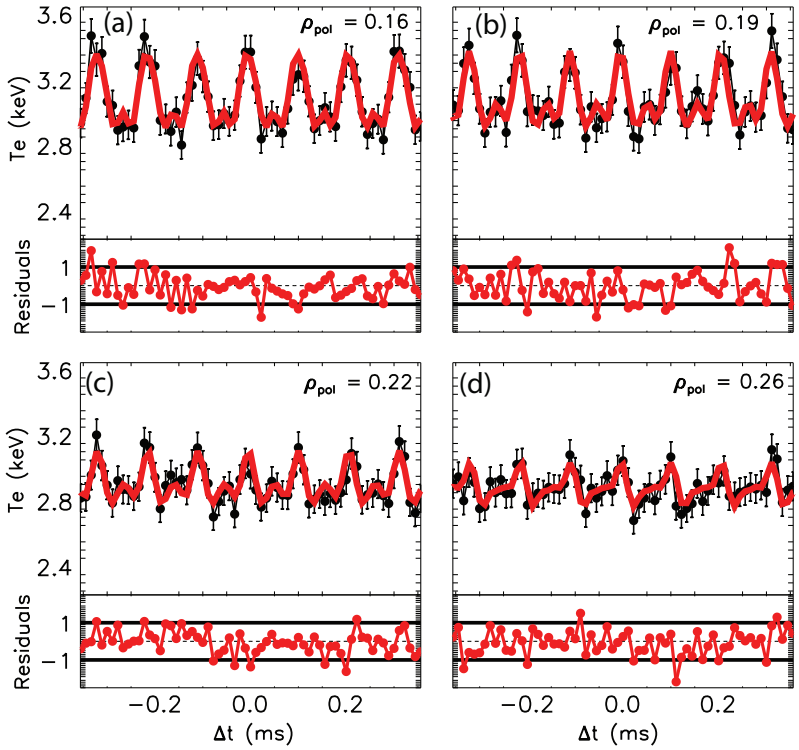

Figure 7. Time reconstruction of the ECE data of four channels (a through d, radial position labeled on of each plot) at t_0 (as labeled close to the dashed vertical line in figures 6a-f): ECE data is shown as black full circles with error bars, the reconstruction as a thick red line. The residuals of the reconstruction are shown in the bottom part of each plot.

oscillations are shown in figures 6g and 6h and for which the time reconstruction of the ECE data is shown in figure 7.

The time-points at saturation $t_2 \rightarrow t_4$ are all within half a mode rotation, showing the different mode phases as they occur at the toroidal location of the SXR diagnostic. Common to all the 2D plots shown in figure 8 is the maximum of the ECRH power density (dashed black contour line, as labeled in 8a) and the inversion radius (thick continuous white contour line, as labeled in 8a). Both have been projected 360° poloidally using the axisymmetric equilibrium to show their position on the poloidal plane for the different phases of the mode. The deposition position of the ECCD (see figures 5 and 6) approximately coincides with the inversion radius. Furthermore, all surface plots apart from the SXR tomography are truncated for $\rho < min(\rho_{ECE}) = 0.16$ (central white region) and outside of a chosen radius (slightly larger than ρ_{inv}) for best plot contrast in the region of interest.

The isothermal surfaces in the 2D plots of the electron temperature at t_1 just after the sawtooth crash (figure 8a) are quasi-concentric, indicating either that the plasma has relaxed back to an axisymmetric case, or that the gradients in the electron temperature after the crash are too shallow for the mode's presence to generate oscillations in the electron temperature detectable by the ECE diagnostic.

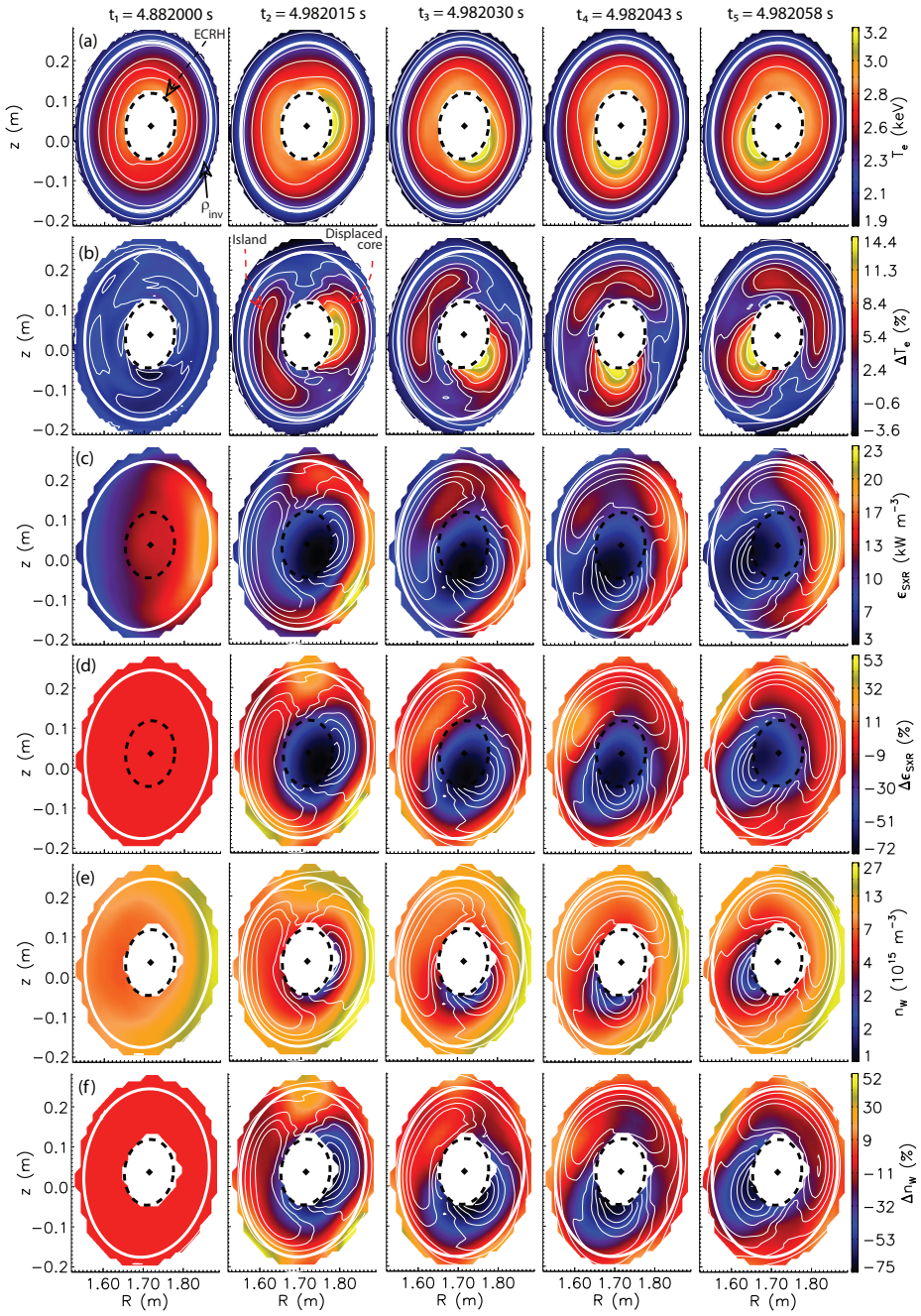

Figure 8. 2D profiles at times $t_1 - t_5$ of: (a) absolute value of the T_e; (b) percentage change in electron temperature with respect to t_1; (c) SXR tomography; (d) percentage change SXR emissivity with respect to t_1; (e) W density; (f) percentage change in W density with respect to t_1. Contours on (c)-(f) are those of the percentage change in the electron temperature for correlation with the mode structure.

During the saturation phase (figure 8a, $t_2 \rightarrow t_4$) the perturbation is clearly visible, a peak in electron temperature rotating clockwise starting at the low-field-side (LFS) midplane at t_2 and proceeding towards the high-field-side (HFS) midplane. Assuming that the electron temperature is constant on the displaced flux surfaces, the shape of the T_e contours will correspond to that of the magnetic flux surfaces. These isothermal contours are concentric a few contour levels inside the inversion radius, indicating that the $q = 1$ surface is located a few centimeters inside ρ_{inv}.

To better resolve the structure of the mode, the evolution of the electron temperature has been plotted with respect to the flux-surface-averaged value (continuum component of the Fourier transform) at t_1, i.e. $\Delta T_e(t) = T_e(t) - \langle T_e(t_1) \rangle$ (figure 8b). With this perspective the perturbation is almost indistinguishable at t_1, while the shape of the mode is now very clear during the saturation phase. The displaced core can now be clearly distinguished from the magnetic island (as labelled on time-point t_2 in figure 8b). The displaced core of the $(1, 1)$ mode exhibits quasi circular flux-surfaces (the isothermal contours) and its temperature has increased of $\sim 14\%$ with respect to the start of the cycle, fourfold with respect to the temperature inside the magnetic island. The island is what one might call a "*hot island*", the temperature increasing when moving from the X-point towards the O-point. For time-points $t_2 \rightarrow t_5$ in figures 8c-e, the contours of the background subtracted electron temperature are over-plotted to the surface plots of the various quantities to correlate them with the mode structure.

The mode structure can now be correlated with the features visible in the SXR tomographic reconstructions (figure 8c). The emissivity is clearly poloidally asymmetric, consistent with a LFS accumulation due to centrifugal effects, for all time-points around the inversion radius, but visible in the reference time-point t_1 for smaller radii as well since no other asymmetries are present. The SXR emissivity profile is otherwise flat just after the sawtooth crash (at t_1) and develops a hollowness which rotates consistently with the displaced core. By subtracting the emissivity just after the sawtooth crash (t_1) form the other frames, the centrifugal asymmetry can be filtered out (figure 8d). The hollowness inside the displaced core is now even clearer, while the emissivity inside the island is relatively flat. With respect to the reference t_1, the emissivity drops of $\sim 70\%$ inside the displaced core while remains approximately unaltered inside the island.

Finally, after having calculated the SXR-filtered W cooling factor using the 2D electron temperature profiles (figure 8a) and solving equation 1 in the $[R, z]$ plane, the 2D mode-resolved W density has been evaluated (figure 8e, plotted on a logarithmic colour scale to provide better contrast with respect to the large, asymmetric W density close to the inversion radius). Excluding the unresolved most central region of the plasma, the W density inside the inversion radius is relatively flat at the start of the sawtooth cycle (t_1 in figure 8e) and exhibits the same asymmetric features seen in the SXR emissivity plots. This asymmetry is conserved during mode saturation ($t_2 \rightarrow t_4$) close to the inversion radius, but inside the inversion radius the W density is now hollow, this *impurity hole* rotating in unison with the displaced core. As performed for the SXR emissivity plots (figure 8d), the asymmetry has been filtered out by plotting the percentage change in W density with respect to the reference time-point t_1 (figure 8f). As for the SXR emissivity, the W density is found to be strongly hollow inside the displaced core, while the island exhibits a flat density profile which is relatively unchanged with respect to the reference time.

The structures observed in both the SXR emissivity and in the W density are very different from what would be expected from a *snake*, a $(1,1)$ helical structure which is seen to occur after pellet injections (of either deuterium/hydrogen or impurity ions) or in the presence of impurity accumulation (see e.g. [56–61]). For the $(1,1)$ snake, the observed SXR signature is that of a sharp peak in the emissivity caused by density accumulation which persists for times of the order to the neoclassical electron diffusion time. This accumulation is thought to take place at the O-point of the $(1,1)$ island. The case presented here is instead characterised by an *impurity hole* in displaced core, while the W density inside the island is flat.

Sawtooth cycles as the one analysed here take place in almost all AUG discharges when ECRH is applied just inside the $q = 1$ surface. While the ECRH deposition position remains constant throughout the whole discharge, the expansion and shrinking of the $q = 1$ surface during to the ECCD sweep changes the relative position of the ECRH and the $q = 1$ surface. With respect to cases where the ECRH is deposited further inwards, this is the case for which the plasma region exhibiting hollow W profiles is found to be the largest (see mode-averaged profiles in figure 5c). The position of the $q = 1$ surface has been estimated as explained in section 4 assuming $\rho_{inv} \sim \sqrt{2}\rho q = 1$, leading to a value of $\rho_{q=1} \sim 0.28$. This position is a good estimate since it also coincides with that of the local minima of the electron temperature oscillation amplitude $\delta T_{e,k=1}$ (figure 6g) and from the $\sim \pi$ phase-jump in the phase $\cos(\varphi_{k=1})$ of the first harmonic $k = 1$ (figure 6h) which is expected to occur close to $\rho_{q=1}$ in the presence of a magnetic island.

6. Summary and conclusions

A comprehensive investigation of the plasma dynamics in the presence of internal $(m,n) = (1,1)$ MHD activity in tokamaks requires the use of different diagnostic systems for an integrative approach. While the characterisation of individual quantities such as the plasma emissivity in the SXR region, the electron temperature and the electron density can be performed with the use of a single diagnostic (SXR, ECE or ECEI and fast-sweeping X-mode reflectometry, respectively), the analysis of the impurity density requires a simultaneous and combined use of all these tools.

In this contribution, a new integrated approach for the evaluation of the mode-resolved 2D impurity density has been explained and applied to the case of intrinsic W in AUG plasmas in the presence of long lasting $(1,1)$ modes occurring in-between sawtooth crashes. Since 2D maps of Z_{eff} and of the main ion density are diagnostically not feasible at the moment, the application of the method requires that W dominates the SXR emissivity such that contributions from other ions can be neglected. If this boundary condition is met, the W density can be calculated from a combined use of SXR tomography and rotation tomography of 1D ECE and fast-sweeping X-mode reflectometry data. Since the latter exhibits a detection limit of $n_e < 5 \cdot 10^{19}\ m^{-3}$ it could not be applied to the discharge under consideration. On the other hand, since the mode-averaged electron density in the given example is relatively flat inside the inversion radius, the density perturbation has been assumed to be negligible and the 1D electron density profiles have been used for the calculation of the mode-resolved 2D W density.

An example reconstruction has been given for a typical lower-single-null AUG H-mode discharge ($q_{95} = 4$, $P_{NBI} = 7.5\ MW$, $P_{ECRH} = 1.4\ MW$). The ECRH power has been delivered using two gyrotrons. By keeping one of them fixed approximately

in the plasma centre and sweeping the second one (set for co-ECCD) from inside to outside of the $q = 1$ surface, the sawtooth-averaged temperature profiles have been kept almost constant, while the sawtooth period and the MHD activity in-between crashes has been drastically altered. Despite the variations in sawtooth period and MHD activity, all sawtooth crashes are found to be *standard* in the electron temperature (peaked profiles before the crash), but *inverted* in the impurity density (hollow before the crash).

Analysing one of these cycles in 2D reveals that this hollowness is located inside the displaced core of the $(1, 1)$ mode. This *impurity hole* is rotating in the laboratory frame in unison with the displaced core of the $(1, 1)$ and exhibits a W density which is $\sim 70\%$ smaller than the values after the sawtooth crash. The magnetic island exhibits instead a flat W density distribution, approximately unaltered with respect to the levels just after the crash. These patterns are very different from what has been observed in the case of *snakes*, since no sharp peak in the SXR emissivity is visible and no W accumulation is taking place at the O-point of the $(1, 1)$ island.

Uncertainties in the evaluation of the W density come from the absence of a mode-resolved 2D electron density measurement, of a trustworthy experimental Z_{eff} profile and from the W atomic data. Since the mode averaged electron density is relatively flat inside the inversion radius, the former can be neglected. Contributions from low-Z impurities and deuterium to the SXR emissivity may instead alter the results more than what shown here (figure 5c). If the low-Z impurity density profile is flat inside the q=1 surface, as already shown in the 1D W density profiles for $Z_{eff} = 1.3$ (figure 5c) would increase the gradients of the W density and would therefore lead to a larger hollowness inside the displaced core. The largest unknown comes form the atomic data. If the shape of the SXR radiation loss parameter were not trustworthy as assumed here, the results could change substantially. With the available experimental and theoretical tools, this cannot at the moment be quantified.

On the other hand, the depth of the hollowness inside the displaced core is such that there seem to be no room for doubt that the observed *impurity hole* is real and not a diagnostic construction. The fact that this *impurity hole* occurs inside the displaced core of the $(1, 1)$ mode and in the presence of ECRH heating inside the $q = 1$ surface opens up new interesting questions that should be tackled in the near future if the mitigation of W accumulation by ECRH is to be understood and its effects extrapolated to future machines such as ITER and DEMO:

- is the saturated mode a *conditio sine qua non* for the W hollowness or only a side-effect of the ECRH heating?
- how do ECRH and MHD concur (if at all) in expelling W from the plasma centre?
- how do neoclassical and turbulent impurity transport change inside the helical $(1, 1)$ core?
- how does impurity transport change in the presence of the magnetic island?
- what is the stability of the long-living $(1, 1)$ modes taking place in the presence of ECRH inside the $q = 1$ surface?
- why isn't the W density profile hollow (and only flat or slightly peaked) when the W accumulation is successfully mitigated using ICRH [36]?

From the experimental point of view, new discharges with lower electron density are planned at AUG in the near future. This will not only enable the use of the fast-sweeping X-mode reflectometry for the determination of the mode-resolved 2D electron

density, but will also provide a parameter scan in electron and ion temperature (and their ratio) for theoretical investigations of impurity transport.

Acknowledgments

This work has been carried out within the framework of the EUROfusion Consortium and has received funding from the Euratom research and training programme 2014-2018 under grant agreement No 633053. The views and opinions expressed herein do not necessarily reflect those of the European Commission.

References

[1] von Goeler S *et al* Nov 1974 *Phys. Rev. Lett.* **33** 1201–1203
[2] Pfeiffer W *et al* 1985 *Nuclear Fusion* **25** 655
[3] Edwards A W *et al* Jul 1986 *Phys. Rev. Lett.* **57** 210–213
[4] Hastie R *et al* 1988 *Nuclear Fusion* **28** 585
[5] Porcelli F 1991 *Plasma Physics and Controlled Fusion* **33** 1601
[6] Yamada M *et al* 1994 *Physics of Plasmas (1994-present)* **1** 3269–3276
[7] Wesson J A *et al* Dec 1997 *Phys. Rev. Lett.* **79** 5018–5021
[8] Reimerdes H *et al* 2000 *Plasma Physics and Controlled Fusion* **42** 629
[9] Furno I *et al* 2001 *Nucl. Fusion* **41** 403
[10] Weisen H *et al* 2001 *Nuclear Fusion* **41** 1227
[11] Letsch A *et al* 2002 *Nuclear Fusion* **42** 1055–1059
[12] Udintsev V S *et al* 2005 *Plasma Physics and Controlled Fusion* **47** 1111
[13] Mück A *et al* 2005 *Plasma Physics and Controlled Fusion* **47** 1633–1655
[14] Lazarus E A *et al* 2007 *Physics of Plasmas (1994-present)* **14** –
[15] Igochine V *et al* 2007 *Nuclear Fusion* **47** 23–32
[16] Papp G *et al* 2011 *Plasma Physics and Controlled Fusion* **53** 065007
[17] Lauret M *et al* 2012 *Nuclear Fusion* **52** 062002
[18] Cecconello M *et al* 2015 *Nuclear Fusion* **55** 032002
[19] Ingesson L C *et al* Feb 2008 *Fusion Science and Technology* **53** 528–576 ISI Document Delivery No.: 266AATimes Cited: 2Cited Reference Count: 277
[20] Nagayama Y *et al* 1990 *Review of Scientific Instruments* **61** 3265–3267
[21] Sertoli M *et al* 2013 *Nuclear Fusion* **53** 053015
[22] Nicolas T *et al* 2012 *Physics of Plasmas* **19** 112305
[23] Park H K *et al* May 2006 *Phys. Rev. Lett.* **96** 195003
[24] Munsat T *et al* 2007 *Nuclear Fusion* **47** L31
[25] Xu X *et al* 2010 *Plasma Physics and Controlled Fusion* **52** 015008
[26] Mattioli M *et al* 1998 *Nuclear Fusion* **38** 189
[27] Giroud C *et al* 2007 *Nuclear Fusion* **47** 313
[28] Parisot T *et al* 2008 *Plasma Physics and Controlled Fusion* **50** 055010
[29] Guirlet R *et al* 2010 *Nuclear Fusion* **50** 095009
[30] Menmuir S *et al* 2010 *Plasma Physics and Controlled Fusion* **52** 095001
[31] Delgado-Aparicio L *et al* 2009 *Nuclear Fusion* **49** 085028
[32] Valisa M *et al* 2011 *Nuclear Fusion* **51** 033002
[33] Sertoli M *et al* 2011 *Plasma Physics and Controlled Fusion* **53** 035024
[34] Sertoli M *et al* 2015 *Plasma Physics and Controlled Fusion* **57** 075004
[35] Odstrcil M *et al* 2012 *Nuclear Instruments and Methods in Physics Research Section A: Accelerators, Spectrometers, Detectors and Associated Equipment* **686** 156 – 161
[36] Dux R *et al* 2003 *Plasma Physics and Controlled Fusion* **45** 1815–1825
[37] Puiatti M E *et al* 2006 *Phys. Plasmas* **13** 042501
[38] Leigheb M *et al* 2007 *Plasma Physics and Controlled Fusion* **49** 1897
[39] Hong J *et al* 2015 *Nuclear Fusion* **55** 063016
[40] Günter S *et al* 1999 *Nuclear Fusion* **39** 1535–1539
[41] Nave M F F *et al* 2003 *Nuclear Fusion* **43** 1204–1213
[42] Pütterich T *et al* 2013 *Plasma Physics and Controlled Fusion* **55** 124036
[43] Asmussen K *et al* 1998 *Nuclear Fusion* **38** 967–986

[44] Mallat S *A Wavelet Tour of Signal Processing, Third Edition: The Sparse Way.* Academic Press, 2008
[45] Horváth L Short time Fourier transforms in NTI Wavelet Tools Technical Report 593, BME-NTI, Budapest, Hungary, November 2012
[46] Schittenhelm M *et al* 1997 *Nuclear Fusion* **37** 1255–1270
[47] Reich M *et al* 2010 *Fusion Science and Technology* **58** 727
[48] Poli E *et al* 2001 *Computer Phys. Comm.* **136** 90–104
[49] Chapman I T *et al* 2013 *Plasma Physics and Controlled Fusion* **55** 065009
[50] Pütterich T *et al* 2008 *Plasma Physics and Controlled Fusion* **50** 085016
[51] Fischer R *et al* 2010 *Fusion Science and Technology* **58** 675–684
[52] Rathgeber S K *et al* 2013 *Plasma Physics and Controlled Fusion* **55** 025004
[53] Willensdorfer M *et al* 2012 *Review of Scientific Instruments* **83** 023501
[54] Mlynek A *et al* 2011 *Nuclear Fusion* **51** 043002
[55] Gude A *et al* Hollow central radiation profiles and inverse sawtooth-like crashes in ASDEX Upgrade plasmas with central wave heating in *Europhysics Conference Abstracts (CD-ROM, Proc. of the 37th EPS Conference on Plasma Physics, Dublin, Ireland, 2010)*, edited by McKenna C, volume 34A of *ECA*, page P4.124, Geneva, 2010, European Physical Society
[56] Weller A *et al* Nov 1987 *Phys. Rev. Lett.* **59** 2303–2306
[57] Gill R *et al* 1992 *Nuclear Fusion* **32** 723
[58] Wesson J A 1995 *Plasma Physics and Controlled Fusion* **37** A337
[59] Naujoks D *et al* 1996 *Nuclear Fusion* **36** 671–687
[60] Pecquet A L *et al* 1997 *Nuclear Fusion* **37** 451
[61] Delgado-Aparicio L *et al* Feb 2013 *Phys. Rev. Lett.* **110** 065006